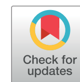

Large enhancement of thermoelectric performance in MoS_2/*h*-BN heterostructure due to vacancy-induced band hybridization

Jing Wu[a,b,1], Yanpeng Liu[b,c,d,1], Yi Liu[b,e], Yongqing Cai[f], Yunshan Zhao[b,e,g], Hong Kuan Ng[a,h], Kenji Watanabe (渡邊賢司)[i], Takashi Taniguchi[i], Gang Zhang[j], Cheng-Wei Qiu[b,e,k], Dongzhi Chi[a], A. H. Castro Neto[b,h], John T. L. Thong[b,e,2], Kian Ping Loh[b,c,j,2], and Kedar Hippalgaonkar[a,b,l,2]

[a]Institute of Materials Research and Engineering, Agency for Science, Technology and Research, 138634, Singapore; [b]Centre for Advanced 2D Materials, National University of Singapore, 117546, Singapore; [c]Department of Chemistry, National University of Singapore, 117542, Singapore; [d]Key Laboratory for Intelligent Nano Materials and Devices of Ministry of Education, Institute of Nanoscience, Nanjing University of Aeronautics and Astronautics, Nanjing 210016, China; [e]Department of Electrical and Computer Engineering, National University of Singapore, 117583, Singapore; [f]Joint Key Laboratory of the Ministry of Education, Institute of Applied Physics and Materials Engineering, University of Macau, Taipa, Macau, China; [g]School of Physics and Technology, Nanjing Normal University, Nanjing 210023, China; [h]Department of Physics, National University of Singapore, 117542, Singapore; [i]Advanced Materials Laboratory, National Institute for Materials Science, 1-1 Namiki, Tsukuba 305-0044, Japan; [j]Institute of High Performance Computing, Agency for Science, Technology and Research, 138632, Singapore; [k]Shenzhen University-National University of Singapore Collaborative Innovation Center for Optoelectronic Science and Technology, Shenzhen University, Shenzhen, 518060, China; and [l]Department of Materials Science and Engineering, Nanyang Technological University, 639798, Singapore

Edited by Eva Y. Andrei, Rutgers, The State University of New Jersey, Piscataway, NJ, and approved May 11, 2020 (received for review April 22, 2020)

Local impurity states arising from atomic vacancies in two-dimensional (2D) nanosheets are predicted to have a profound effect on charge transport due to resonant scattering and can be used to manipulate thermoelectric properties. However, the effects of these impurities are often masked by external fluctuations and turbostratic interfaces; therefore, it is challenging to probe the correlation between vacancy impurities and thermoelectric parameters experimentally. In this work, we demonstrate that n-type molybdenum disulfide (MoS_2) supported on hexagonal boron nitride (*h*-BN) substrate reveals a large anomalous positive Seebeck coefficient with strong band hybridization. The presence of vacancies on MoS_2 with a large conduction subband splitting of 50.0 ± 5.0 meV may contribute to Kondo insulator-like properties. Furthermore, by tuning the chemical potential, the thermoelectric power factor can be enhanced by up to two orders of magnitude to 50 mW m^{-1} K^{-2}. Our work shows that defect engineering in 2D materials provides an effective strategy for controlling band structure and tuning thermoelectric transport.

thermoelectric | Kondo | 2D materials | Seebeck | phonon drag

Thermoelectrics are solid state energy converters that can be used to harvest electrical energy from waste heat; thus, they are attractive as a sustainable energy resource. The performance of thermoelectric materials is characterized by the thermoelectric figure of merit (ZT, defined as $S^2\sigma T/\kappa$, where T is the absolute temperature): the key bottleneck is the interdependency between the Seebeck coefficient (S), electrical (σ), and thermal (κ) conductivities. An ideal thermoelectric material should exhibit simultaneously large S and σ (1). It has been proposed that van der Waals materials, in their two-dimensional (2D) form with discretized density of states (DOS) (quantum confinement), may show better performance in thermoelectrics compared to bulk materials (2). For instance, bulk layered SnSe has been found to have a figure of merit (ZT) of 2.8 ± 0.5. The remarkably high ZT is not due to quantum confinement but instead due to the anharmonicity of its chemical bonds, giving it an ultralow thermal conductivity at high temperature (700 to 900 K) (3, 4). However, the power factor (PF = $S^2\sigma$) is still relatively modest (1 mW m^{-1} K^{-2}) (3). New transport mechanisms are needed to push the PF of thermoelectric materials beyond the well-known S-σ anticorrelation limit (1). For example, the violation of the Mott relation results in enhanced PF in the hydrodynamic charge transport regime in graphene due to strong inelastic scattering among electrons (5). It is well known that impurity states, especially magnetic impurities, not only strongly couple with itinerant charge carriers but can also significantly affect the band structure and even reverse charge transport behavior (6–8). Few-atoms-thick layered materials are highly sensitive to such extrinsic effects, and therefore, they serve as a good platform for exploiting thermoelectric properties by introducing such impurities. Among these materials, MoS_2 has attracted special attention because of its well-defined spin-splitting under light illumination and/or applied magnetic fields (9–11). Extrinsic magnetic impurities in MoS_2 can be introduced by vacancies, dislocations, edges, strain, or doping by magnetic ions (12–16). However, due to its extreme sensitivity to external fluctuations and turbostratic interfaces,

Significance

The study of correlated phenomena in 2D semiconductors opens up new pathways toward understanding and engineering material functionalities (such as thermoelectrics) in easily accessible van der Waals solids. Local structural defects such as vacancies inevitably exist in natural as well as synthetic TMD crystals and have been predicted to serve as magnetic impurities capable of enhancing the strongly correlated effect. Herein we discover unusual thermoelectric behavior in sulfur vacancy-enriched MoS_2 by rationally selecting *h*-BN as the substrate. We demonstrate that the thermoelectric transport properties can be strongly manipulated by vacancy-induced Kondo hybridization. A significant enhancement of thermoelectric power factor by two orders of magnitude is achieved in the MoS_2/*h*-BN device.

Author contributions: A.H.C.N., J.T.L.T., K.P.L., and K.H. supervised the projects; J.W., Yanpeng Liu, K.P.L., and K.H. conceived the idea and design the experiment; J.W., Yanpeng Liu, Yi Liu, Y.C., Y.Z., H.K.N., K.W., T.T., G.Z., and K.H. performed research; K.W. and T.T. contributed high-quality hBN substrates; J.W., Yanpeng Liu, Yi Liu, Y.C., Y.Z., H.K.N., C.-W.Q., D.C., A.H.C.N., J.T.L.T., K.P.L., and K.H. analyzed data; and J.W., Yanpeng Liu, Y.C., K.P.L., and K.H. wrote the paper.

The authors declare no competing interest.

This article is a PNAS Direct Submission.

Published under the PNAS license.

[1]J.W. and Yanpeng Liu contributed equally to this work.

[2]To whom correspondence may be addressed. Email: john_thong@nus.edu.sg, chmlohkp@nus.edu.sg, or kedar@ntu.edu.sg.

This article contains supporting information online at https://www.pnas.org/lookup/suppl/doi:10.1073/pnas.2007495117/-/DCSupplemental.

Downloaded at Ukraine: PNAS Sponsored on June 13, 2020

there has not yet been a clear correlation between the thermoelectric properties of layered 2D materials and impurities.

In this work, we report that when few-layer MoS_2 flakes are interfaced to hexagonal boron nitride (*h*-BN) substrate, a correlation between charge carriers and vacancy impurities in MoS_2 is clearly observed. This is in part due to reduced scattering by charged surface states and surface roughness on the atomically smooth and chemically inert *h*-BN substrate. Using low-temperature scanning tunneling microscopy (LT-STM), single-atom sulfur vacancies (up to $\sim 1.81 \pm 0.4 \times 10^{12}$ cm^{-2}) were observed on MoS_2. The conduction subband near the vicinity of such a sulfur vacancy shows a colossal band splitting of 50 ± 5 meV. Density functional theory (DFT) simulations reveal that this band hybridization may originate from sulfur vacancy-induced magnetic states. When fabricated into a MoS_2/*h*-BN field effect transistor (FET) device, we observed an anomalous sign change of the Seebeck coefficient and an extremely large positive Seebeck value (~2 mV/K) even in the metallic regime at 60 K. Furthermore, an electrostatically tunable PF of MoS_2/*h*-BN device larger by two orders of magnitude is achieved due to strong interactions between conducting charges and the observed vacancy states, attaining a value as high as 50 mW m^{-1} K^{-2} in the temperature range from 30 to 50 K. Our results demonstrate that engineering vacancies in 2D layered crystals provide a material platform for next generation thermoelectric and energy applications.

Results

Vacancy-Induced Band Hybridization in MoS_2/*h*-BN Heterostructure. Inversion symmetry breaking at vacancy or edge sites of MoS_2 has been theoretically predicted to enable local magnetic moments and induces band splitting of both valence and conduction bands (17). To probe band splitting induced by vacancies in MoS_2, an atomically flat *h*-BN substrate is employed to avoid spurious effects from impurities at the interfaces. The MoS_2/*h*-BN heterostructure device was fabricated by a well-established transfer technique and then loaded into the LT-STM chamber and annealed in ultrahigh vacuum ($<1 \times 10^{-10}$ torr) to ensure better electrical and thermal contact and a cleaner surface (more details in *SI Appendix*, Notes S1 and S2).

Fig. 1*A* shows a typical STM topographic image of MoS_2 flake on *h*-BN for a scan area of 75 nm × 75 nm at liquid helium temperatures. The thickness of MoS_2 flake was confirmed to be six layers using atomic force microscopy and verified subsequently by scanning tunneling spectroscopy (STS) (Fig. 1*C*). The dark topographic contrast in the STM image (Fig. 1*A*) and lattice discontinuity are hallmarks of single sulfur vacancies (18), with a concentration of $\sim 1.81 \pm 0.4 \times 10^{12}$ cm^{-2}. In the high-resolution image inserted in Fig. 1*C*, *Center*, a hexagonal lattice with a periodicity of 3.15 ± 0.5 Å is seen (*SI Appendix*, Fig. S3), corresponding to the atomic lattice of the top sulfur layer in the MoS_2 crystal (19). The defects are experimentally observed at the center of sulfur lattice sites, excluding other defect types such as interstitials, Mo vacancy, or antisite defects (a Mo atom substituting a S_2 column or vice versa) (20). STS, which probes the local density states, was applied to study the effect of such sulfur vacancy defects on the electronic properties. To better resolve the effect of sulfur vacancies, a lower set point ($V_S = -0.7$ V, I = 1.3 nA) was used to collect the dI/dV spectrum from the vicinity of sulfur vacancy as well as far away from it (Fig. 1*C*). At regions where the MoS_2 is pristine (Fig. 1*C*, Center), a series of oscillation peak/dip features were observed at the conduction band region spaced ~98.0, ~134.3, and ~169.0 meV apart, in good agreement with the subband (C_1, C_2, and C_3; Fig. 1*C*, Right) structure of six-layer MoS_2 predicted by DFT calculations. Intrinsically, such subbands are associated with quantum confinement of electronic states. When the STM tip is located on top of a vacancy, however, a splitting (energy of 50.0 ± 5.0 meV) of these subbands (into C_{1a} and C_{1b}, C_{2a} and C_{2b}, and C_{3a} and

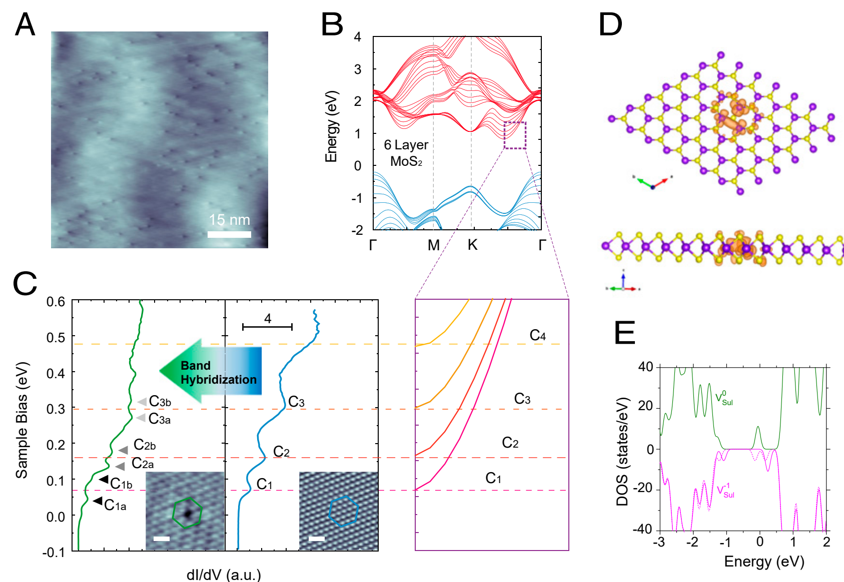

Fig. 1. Electronic properties and band structure of six-layer MoS_2 with sulfur vacancy. (*A*) Large-area STM image of the bare MoS_2 on *h*-BN substrate (V_S = 1.0 V, I = 0.7 nA). The dark topographic contrast, which shows the single sulfur vacancy features, can be found over the whole scanned area. (*B*) DFT calculation of six-layer MoS_2. The zoomed-in image shows the conduction subbands (C_n) near the CBM at point of six-layer MoS_2. (*C*) *dI/dV* spectrum ($V_S = -0.7$ V, I = 1.3 nA) at the vicinity of a sulfur vacancy (*Left* side) (scale bar, 0.6 nm) and pristine region (*Right*) (scale bar, 0.8 nm) of MoS_2 near CBM. Conduction subbands C_1, C_2, and C_3 can be revealed from the resonance peaks in STS curve of pristine MoS_2. However, each of those subbands split into two bands (C_{na} and C_{nb}) due to band hybridization in the vicinity of a sulfur vacancy. (*D*) Top and side views of spin density associated with single sulfur vacancy in monolayer MoS_2. (Purple larger spheres represent molybdenum atoms, and smaller yellow spheres represent sulfur atoms.) The spin density associated with $V_{Sul}{}^{-1}$, with a significant component localized at the three exposed Mo atoms. (*E*) Electronic DOS of the sulfur vacancy in neutral ($V_{Sul}{}^{0}$) and −1 charged state ($V_{Sul}{}^{-1}$) (for intuitive understanding, the VBMs for the two cases were aligned).The charging of the vacancy leads to the lifting of the degeneracy of defective level indicated by the splitting of curves of spin-up (dashed line) and spin-down (solid line) states for $V_{Sul}{}^{-1}$.

Downloaded at Ukraine: PNAS Sponsored on June 13, 2020

C_{3b}) was clearly captured, which is similar to observations of band hybridization in Kondo insulators (21). A survey scan using X-ray photoelectron spectroscopy over the whole MoS_2 flake shows no evidence of magnetic elemental impurities (*SI Appendix*, Fig. S4).

In order to investigate the local effect of vacancies on electronic structure in MoS_2, first-principle calculations were conducted on monolayer MoS_2 (more calculation details in *SI Appendix*, Note S4). The removal of one sulfur atom in the MoS_2 sheet creates a single sulfur vacancy (V_{Sul}), accompanied by dangling states and exposure of Mo atoms in the vacancy core. Single neutral V_{Sul} has two states: a fully occupied singlet A state and an empty doubly degenerate E state (22). When carriers are injected into the MoS_2, the V_{Sul} state becomes negatively charged, and the ${V_{Sul}}^{-1}$ is spin-polarized, accompanied by a spin moment of $\mu = 1/2$. The spin density associated with ${V_{Sul}}^{-1}$, with a significant component localized at the three exposed Mo atoms, is shown in Fig. 1 *D* and *E*. Charging via gating alters the local magnetic moment and state-splitting of the V_{Sul}, which in turn, tunes the scattering of charge carriers, especially at low temperatures (23).

Electrical Performance Due to Band Hybridization. To investigate the influence of vacancy-induced band hybridization, temperature-dependent transport measurements were carried out. Fig. 2*A* shows the top and section view of the MoS_2/*h*-BN heterostructure, and a representative optical image is shown in Fig. 2*B*. To be consistent, a MoS_2 flake with thickness 4.2 ± 0.3 nm was selected (six layers; Fig. 1*C*) (more transport results of various thicknesses are provided in *SI Appendix*, Note S15). Four-probe measurements were performed to exclude the effects of electrical contact resistance, and the nanofabricated heater allows thermoelectric measurements. The linear I_{sd}–V_{sd} curves collected at room temperature (Fig. 2*C*) indicate ohmic contacts between metal electrode and MoS_2 flake (*SI Appendix*, Fig. S6). The carrier concentration (n) in MoS_2 is modulated by applying a back-gate voltage (V_g). Fig. 2*D* shows an increasing conductance (G) with V_g for the MoS_2/*h*-BN sample within the measured temperature (T) range, indicating typical n-type FET behavior. From 300 to 100 K, a clear crossing point (at $V_g \sim 20$V) appeared, indicating that MoS_2 undergoes a routine metal-to-insulator transition (MIT), where the conductance changes from decreasing with temperature to increasing with temperature (24–26). At $T < 100$ K, the conductance drops anomalously as T decreases, in contrast with the trend exhibited by MoS_2 on Si/SiO_2 devices. This can be explained by the strong hybridization between localized impurities states and conduction electrons, which will be further discussed later.

In order to better understand the electronic transport in MoS_2/*h*-BN, temperature-dependent four-probe sheet conductivity ($\sigma_s = G{\cdot}L/W$, where L and W are the length and width of sample channel, respectively) was plotted as a function of V_g for both MoS_2/*h*-BN (Fig. 3*A*) and MoS_2/SiO_2 (Fig. 3*B*) devices for comparison. In the high temperature range ($T > 100$ K), and close to $\sigma_s \sim e^2/h$, the metal-insulator transition driven by electron correlations can be observed clearly in both devices. For MoS_2/SiO_2 device, such behavior exists over the temperature range from 300 to 20 K. However, for the MoS_2/*h*-BN device, instead of saturating at a residual value as $T \rightarrow 0$, a conductance peak (temperature at this critical point is defined as T_{max}; red dashed line in Fig. 3*A*) in the metallic region is observed. This observed anomalous resistance minimum at low temperature is another signature of a Kondo insulator behavior.

This effect is suppressed in the MoS_2/SiO_2 device due to the imperfect interface between MoS_2 and SiO_2 but clearly detectable for the six-layer MoS_2/*h*-BN devices (more data on six-layer

APPLIED PHYSICAL SCIENCES

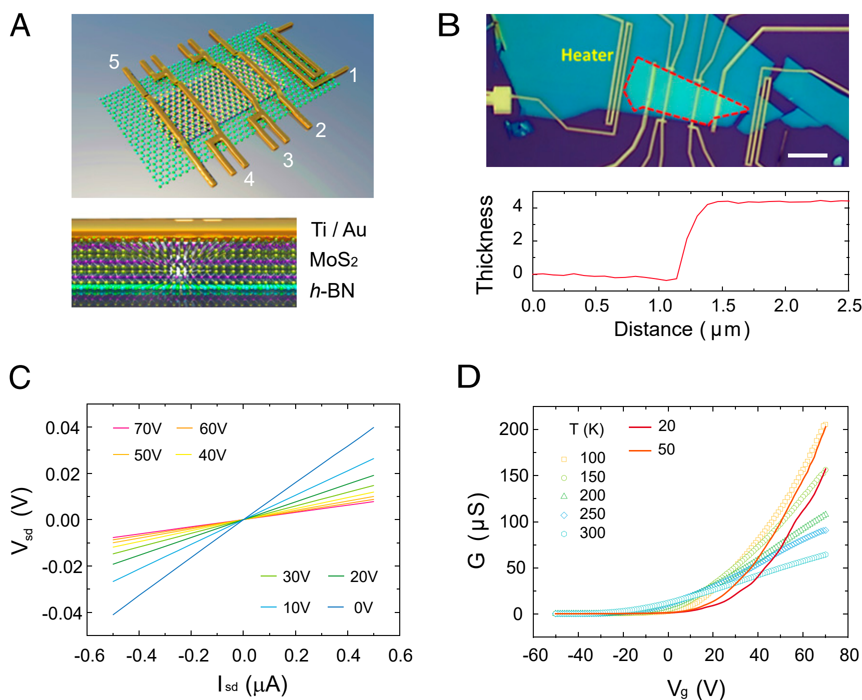

Fig. 2. Structural and electronic properties of MoS_2/*h*-BN heterostructure. (*A*) Schematic diagram of the device. Electrode 1 acts as an electrical heater. Electrodes 2 and 5 act as a current source for four-probe electrical measurements, while electrodes 3 and 4 act as thermometers. (*Bottom*) The section view of the heterostructure. (*B*) Optical image of a complete device. The dotted red dashed box outlines the MoS_2 flake. (Scale bar, 10 μm.) (*Bottom*) AFM scan gives the thickness of MoS_2 flakes as 4.2 ± 0.3 nm. (*C*) Four-probe I_{sd}-V_{sd} curves at different V_g values at 300 K. (*D*) Four-probe FET characterization at different temperatures. Clear crossover can be found at $V_g \sim 20$V for $T > 100$ K, which is defined as the MIT. For $V_g > V_{MIT}$, MoS_2 shows metallic behavior, and conductance decreases with increasing T. For $V_g < V_{MIT}$, conductance increases with increasing T, which is a typical insulating behavior. When $T < 100$ K, the conductance (in the metallic region) drops anomalously as T decreases.

Downloaded at Ukraine: PNAS Sponsored on June 13, 2020

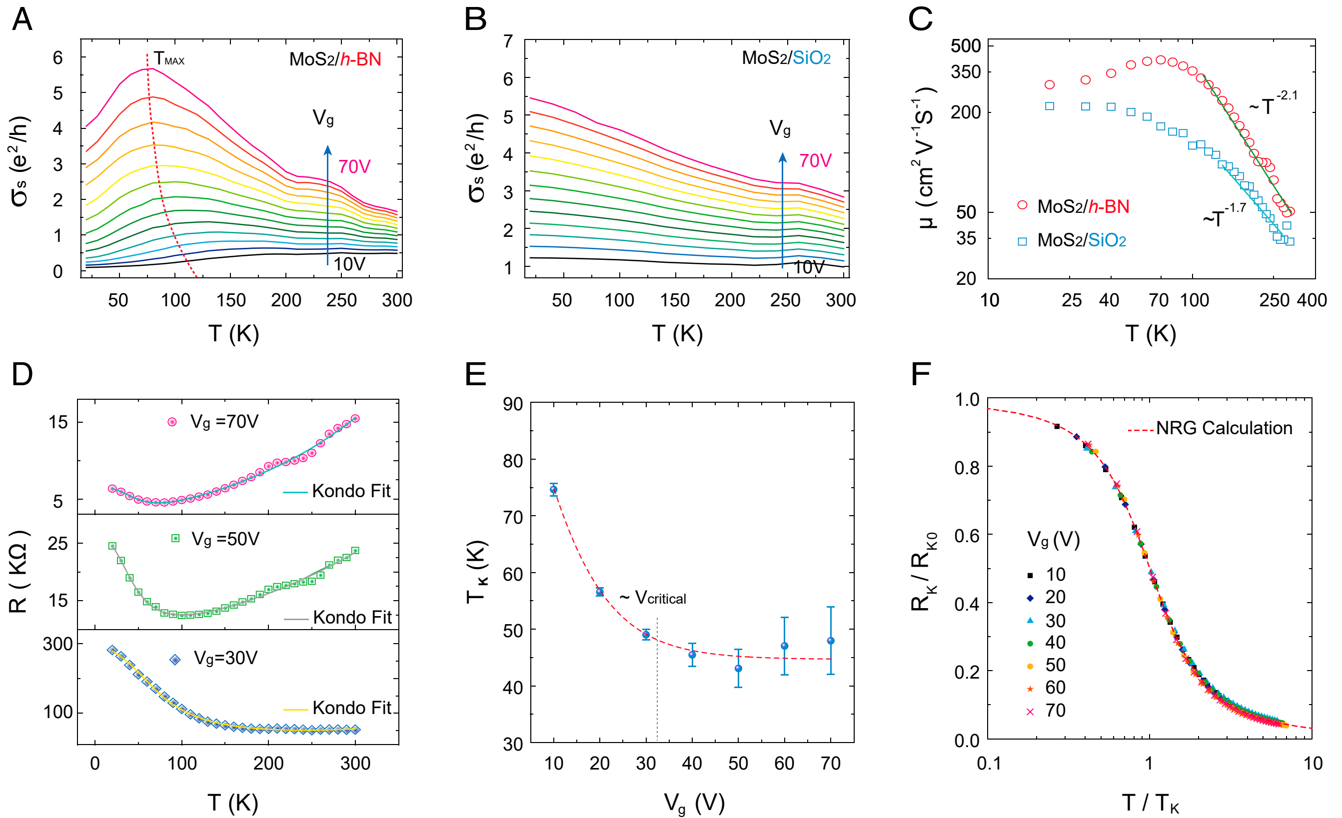

Fig. 3. Carrier density and temperature-dependent properties of defective MoS_2 on *h*-BN substrate. (*A*) Four-probe sheet conductivity of MoS_2/*h*-BN devices as a function of T and V_g. MIT can be observed when $\sigma_s \sim e^2/h$. The anomalous peaks T_{max} at low temperatures are marked out by the red dashed line. (*B*) Four-probe sheet conductivity of MoS_2/SiO_2 devices as a function of T and V_g. (*C*) Temperature-dependent field effect mobility. The solid line shows the phonon-limited power law $\mu_{ph} \sim T^{-\gamma}$. $\gamma = 1.7$ and $\mu \sim 200$ $cm^2V^{-1}s^{-1}$ for MOS_2/SiO_2 sample. For MoS_2 on *h*-BN, $\gamma = 2.1$ and μ reaches 405 $cm^2V^{-1}s^{-1}$. For $T < 100$ K, $d\mu_{FE}/dT > 0$ is observed for MoS_2/*h*-BN sample indicating an anomalous scattering mechanism. (*D*) Temperature dependence of four-probe resistance at V_g = 70, 50, and 30 V for MoS_2/*h*-BN device, with the resistance minima at 70, 89, and 135 K, respectively. (*E*) Gate tuning of the Kondo temperature T_k. (*F*) Normalized Kondo resistance versus normalized temperature for the data from V_g = 10 V to V_g = 70 V. The red dashed line describes the universal Kondo behavior from numerical renormalization group calculations (35).

MoS_2/SiO_2 and MoS_2/*h*-BN as well as monolayer and bilayer MoS_2/*h*-BN are in *SI Appendix*, Note S15). At low temperatures, the hybridization of the conduction band with the localized impurity state manifests in a large band splitting. Kondo resonant scattering can dominate charge transport in this temperature range and give rise to the anomalous component of the resistance. Such a picture is also complemented by the change in four-probe mobility (μ) with temperature (Fig. 3*C*). For MoS_2 on SiO_2, μ is mainly limited by optical phonon scattering when $T > 100$ K, and its temperature dependence follows a power law of $\mu \sim T^{-\gamma}$ (27). Once $T < 100$ K, most optical phonons are deactivated, and saturation is observed, resulting in $d\mu/dT \sim 0$ as $T \rightarrow 0$ (27). On the contrary, MoS_2/*h*-BN device deviates from this trend where its mobility decreases as $T <$ 100 K and shows $d\mu/dT > 0$.

Fig. 3*D* shows the four-probe resistance plots of MoS_2/*h*-BN device at three different back gates. For each curve, a clear resistance minimum can be observed at 70, 89, and 135 K. For a better understanding of this data, apart from 2D Block–Gruneisen resistance $(\propto T^4)$ (28, 29) and electron–phonon high temperature resistance $(\propto T)$, we employ a Kondo resistance model [$R_K(T_K, T)$, full expression in *SI Appendix*, Note S11]:

$$R = AT^4 + BT + R_K(T_K, T) + R_0, \quad [1]$$

where R_0 is the temperature-independent term arising from a residual zero temperature resistance (Fig. 3*D*). In the Kondo picture, close to a characteristic temperature (Kondo temperature, T_K), magnetic impurities quantum-mechanically exchange spin with conduction electrons of many wave vectors (momenta) (30), thereby creating a resonant scattering state at the Fermi level with a width $\sim k_B T_K$ [$k_B T_K \sim \Delta \exp\left(\frac{-1}{D(E_F)J_0}\right)$, where $D(E_F)$ is the electron DOS at the Fermi level, Δ is the bandwidth, and J_0 is a constant representing a Kondo scattering exchange energy] (31, 32). As a result, a dip in the resistance vs. temperature curve appears. Fig. 3*E* summarizes the T_K variation as a function of V_g for MoS_2/*h*-BN sample. At $V_g > V_{MIT}$, T_K remains nearly unchanged because of the constant 2D DOS. When $V_g < V_{MIT}$, the Fermi level shifts toward the gap region; therefore, T_K starts to increase with lower doping, similar to the behavior observed in heavily doped fermion bulk systems such as $CePd_3$ (33). We also scale the $R(T)$ curves at each V_g and observe a universal Kondo behavior (6, 34), in which the normalized Kondo resistance R_k/R_{k0} vs. T/T_k at all gate voltages collapses onto a single universal Kondo behavior curve (Fig. 3*F*). This is in accordance with numerical renormalization group theory (35), which attests to the Kondo-driven transport in MoS_2/*h*-BN devices.

Thermoelectric Performance Driven by Band Hybridization. To investigate further if the thermoelectric values show a similar effect, a DC current is introduced via a nanofabricated heater to create a temperature gradient along the devices (Fig. 2*A*). Fig. 4*A* shows the Seebeck coefficient (S) as a function of temperature at V_g = 70, 50, and 30 V for both MoS_2/*h*-BN and SiO_2

Downloaded at Ukraine: PNAS Sponsored on June 13, 2020

devices. The absolute $|S|$ decreases with increasing carrier concentration in the MoS_2 channel (details in *SI Appendix*, Note S13 and Fig. S19), comparable to the reported trends in earlier work (36, 37). From the temperature-dependent behavior of S for both samples, a clear dip located around 100 to 150 K can be observed which is very close to the thermal conductivity peak of MoS_2 (38, 39), indicating the contribution of acoustic phonons in MoS_2 to the Seebeck coefficient via the phonon drag effect, S_{ph} (40). Both MoS_2/SiO_2 and MoS_2/*h*-BN samples show similar values of negative S and behavior for $T > 120$ K. However, when $T < 120$ K, an anomalous sign change (from negative to positive) in S is observed in MoS_2/*h*-BN sample even though electrons remain as the dominant charge carriers. The positive S reaches a magnitude as high as 2 mV/K for $V_g = 30$ V at 60 K, which is almost one order of magnitude enhancement compared to MoS_2/SiO_2 sample (−270 μV/K) under the same experimental conditions. This is a remarkably large value for a material in the metallic state. To better illustrate the sign change of S, a 2D map of S as a function of both T and V_g is plotted in Fig. 4*B*. Clearly, S changes from negative to positive values at all gate voltages. It is also found that the critical temperature (defined as the temperature at which $S = 0$) and the maximum positive S (highest intensity; red in Fig. 4*B*) increases as V_g decreases, suggesting that the Seebeck coefficient can be tuned by electrostatic gating. Importantly, this critical temperature across all temperatures for $S = 0$ is identical to the conduction maximum line T_{max} in Fig. 3*A*, further evidencing that this anomalous thermoelectric transport has the same origins as the electronic transport.

Since the transfer curve shows unambiguous *n*-type behavior and the quasiparticle bandgap of six-layer MoS_2 is relatively large (41), the valence band states of MoS_2 are inaccessible and hence cannot result in a positive S, especially at low temperatures. When electrons are the majority carriers, the single-particle Boltzmann transport equation (BTE) can be employed to describe thermoelectric transport and is defined as S_{BTE}. In the degenerate state (highly conducting on-state), the BTE reduces to the Mott formula described below (42):

$$S_{BTE} = -\frac{\pi^2}{3}\frac{k_B^2 T}{|e|}\left[\frac{\partial \ln \tau}{\partial E} + \left(\frac{\partial \ln g}{\partial E} + \frac{\partial \ln v^2}{\partial E}\right)\right]\Bigg|_{E=E_F} = S_\tau + S_N, \quad [2]$$

with $S_\tau = -\frac{\pi^2}{3}\frac{k_B^2 T}{|e|}\frac{\partial \ln \tau}{\partial E}\Big|_{E=E_F}$ and $S_N = -\frac{\pi^2}{3}\frac{k_B^2 T}{|e|}\left(\frac{\partial \ln g}{\partial E} + \frac{\partial \ln v^2}{\partial E}\right)\Big|_{E=E_F}$.

Here k_B, τ, g, and v indicate the Boltzmann constant, relaxation time, DOS, and group velocity, respectively. S_τ and S_N are the contributions arising from the energy-dependent scattering and diffusion. The sign of S_N only depends on the charge carrier type; thus, an *n*-type MoS_2 will only exhibit a negative S_N. As such, the Seebeck coefficient (S) comprises the sum of S_{BTE} and S_{ph}. For the MoS_2/SiO_2 sample, the low-temperature thermoelectric transport is dominated by acoustic phonon scattering where the acoustic phonon scattering relaxation time (τ) is energy independent (43) in the 2D limit. Hence, the S_{BTE} of our MoS_2/SiO_2 is dominated by negative S_N and phonon drag S_{ph}. Here S_N can be calculated by solving the linearized BTE under a relaxation time approximation (detailed calculations are provided in *SI Appendix*, Note S12) (36, 44). Consequently, the overall phonon drag Seebeck coefficient ($S_{ph} = S_{total} - S_N$) can be estimated. Fig. 4*C* shows the measured Seebeck coefficient (S) as a function of temperature of MoS_2/SiO_2 device at a carrier concentration of $n = 2 \times 10^{12}$ cm^{-2}. The phonon drag contribution S_{ph} shows clear peaks around 100 K as expected where the largest concentration of heat-carrying phonons (acoustic phonons) can interact with carriers (45). Hence, the peak position is not changing across different back gate voltages (*SI Appendix*, Fig. S18). At temperatures below 100 K, S_{ph} diverges from unity. A first-order quantitative estimation of phonon drag S is given by

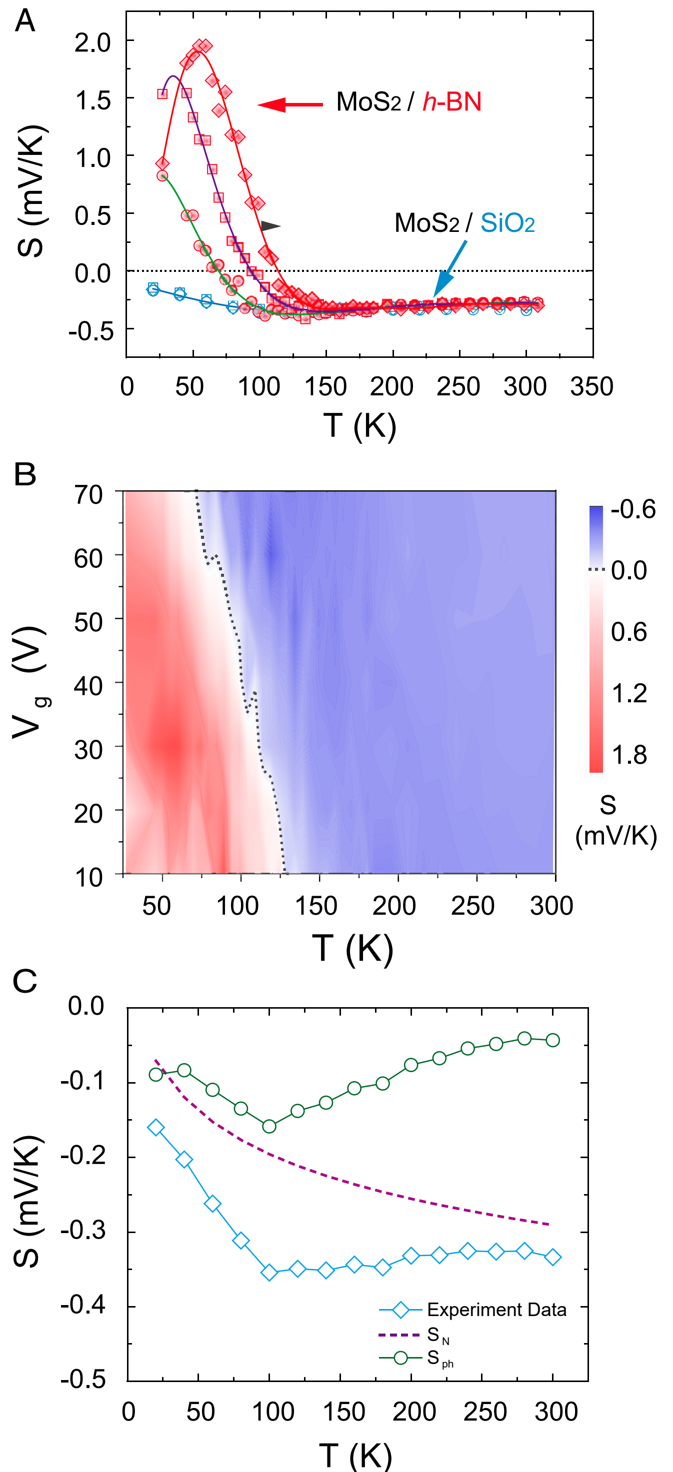

Fig. 4. Thermoelectric transport and Seebeck coefficient measurement of defective MoS_2 on *h*-BN substrate. (*A*) Comparison of S vs. T of MoS_2/SiO_2 and MoS_2/*h*-BN device at $V_g = 70$ V (circle), 50 V(square), and 30 V (diamond) (from left to right; black arrow). The solid lines guide the eye. MoS_2/SiO_2 sample shows negative values due to the diffusive type *n*-type charge carriers. For MoS_2/*h*-BN sample, at low temperatures, an anomalous sign change in S occurs where the majority carriers are electrons. (*B*) Color contour plot of S values versus V_g and T for MoS_2/*h*-BN device. The black dotted line indicates the point with $S \sim 0$ mV/K. (*C*) Total S values of MoS_2/SiO_2 sample at $n = 2 \times 10^{12}$ cm^{-2} and its respective contributions from the energy-dependent diffusion S_N and phonon-drag S_{ph}.

Downloaded at Ukraine: PNAS Sponsored on June 13, 2020

$S_{ph} = \beta v_s l_s / \mu T$ (46–48), where v_s is the velocity of sound and l_s is the phonon mean free path. $\beta \subset (0, 1)$ indicates the relative contribution of electron–phonon interaction to electron mobility. The phonon mean free path can be evaluated using the Debye equation $\kappa = \frac{1}{3} c v_s l_s$, yielding $l_s \sim 5.5$ to 14nm which is consistent with the calculated values from literature (49). We remark that this estimated l_s is an effective lower bound involving all phonons. The resulting estimate of $S_{ph} \sim 10^2 \mu V/K$ is also comparable to our results (details in *SI Appendix*, Note S12).

However, an anomalous sign change in S is observed for the MoS_2/*h*-BN sample accompanied by large positive values in the low-temperature region. Typically, a sign change in S occurs when the type of charge carrier changes, like in ambipolar materials [graphene (50) and black phosphorus (51)] or in complicated Fermi surface nesting systems such as charge density wave phase transition materials [$NbSe_3$ (52) and $TaSe_3$ (53)]. In addition, it has been observed that longer phonon mean free paths such as those in *h*-BN may contribute to an anomalously large thermoelectric behavior through the phonon drag effect (45). In such cases, the phonon drag S_{ph} peak should occur at higher temperatures due to the higher Debye temperature of *h*-BN. On the contrary, the observed peak in S_{total} is located at lower temperatures in our experiments (Fig. 4*A*). Moreover, our experiment further shows that the sign change in S_{total} is strongly dependent on the modulation of electron carrier concentration (gate effect) and vacancy concentration in MoS_2 (controlled via annealing). Hence, the anomalous thermoelectric transport can be mainly attributed to the strong correlation transport induced by the hybridized band structure, as shown in our STS results, in addition to phonon drag in MoS_2.

In fact, the vacancy-induced band hybridization and Kondo effect have been studied in 2D materials like graphene (6, 54, 55). In such a case, the scattering is highly energy-dependent, and the mobility is known to be proportional to $1/\tau$ (56), which is opposite to the conventional one-band system where $\mu \propto \tau$. Approximating $1/\partial E$ as $1/(k_B \partial T)$ (57) in S_τ, $\frac{\partial \ln \tau}{\partial T} \propto -\frac{d\mu}{dT}$ could be derived to describe the relationship between Seebeck coefficient and mobility. From Fig. 5*A*, we can see that the measured S is positive in the region where $\frac{d\mu}{dT} < 0$, in good agreement with the Kondo physics model. In this model, the interaction between electrons at Fermi energy and hybridized band strongly influence the nonequilibrium energy spectrum, thereby generating a Kondo resonance that reverses the sign of Seebeck coefficient. This is further corroborated by the peak position of the S values occurring near the Kondo temperature.

To understand how the S is related to resonant scattering (S_τ), the two-band approach originating from the Hirst model is adopted (58):

$$S_\tau = A \frac{T\varepsilon_0}{\varepsilon_0^2 + [T_\Gamma exp(-T_\Gamma/T)]^2}. \quad [3]$$

Here the conduction electrons are scattered by an extraband induced by the hybridization. This band is described using a Lorentzian form

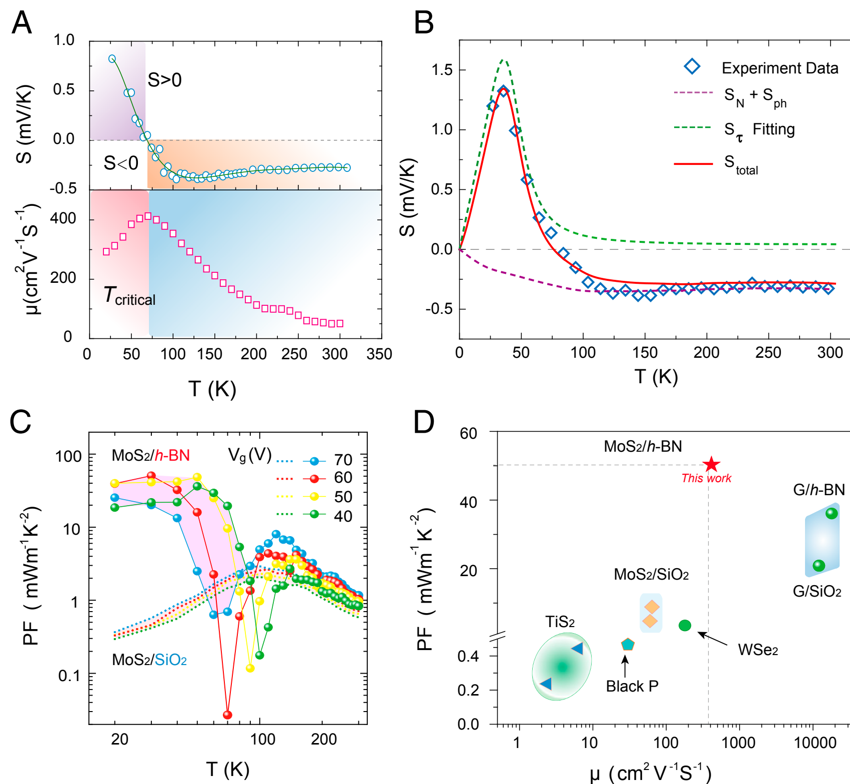

Fig. 5. Thermolectric performance of MoS_2/*h*-BN heterostructure. (*A*) Seebeck coefficient and mobility as function of temperature at $V_g = 70$ V for MoS_2/*h*-BN device. (*B*) Total S values of MoS_2/*h*-BN sample at $n = 2 \times 10^{12}$ cm^{-2} are contributions from the energy-dependent diffusive part S_N, phonon-drag part S_{ph}, and the Kondo scattering part S_τ. At a fixed n, the total S first exhibits a diffusive negative value at high temperatures from conducting electrons described by $S_N + S_{ph}$. As the temperature decreases, the conventional diffusive contribution is weakened, and the Kondo scattering term S_τ starts to dominate and shows large positive values. As temperature is decreased further, all of the physical interactions start to freeze, and the total S goes back to zero as expected (64). (*C*) Comparison of PF of MoS_2/*h*-BN and MoS_2/SiO_2 sample as a function of temperature at different gate voltages. Additional band hybridization-induced peaks as high as 50 mW m^{-1} K^{-2} can be observed at 30 K ~ 50 K for MoS_2/*h*-BN sample. (*D*) The PF value of our MoS_2/*h*-BN heterostructure shows superior thermoelectric performance compared to even the highest reported values in other 2D materials at room temperature. [G/SiO_2 and *h*-BN (50), MoS_2 (36, 37), WSe_2 (60), TiS_2 (61, 62), and BP (51).]

Downloaded at Ukraine: PNAS Sponsored on June 13, 2020

with a width Γ_0 located at ε_0 with respect to the Fermi level. Γ_0 varies with temperature as $\Gamma_0 = T_\Gamma \exp(-T_\Gamma/T)$. T_Γ is a temperature-dependent parameter and represents the quasi-elastic linewidth of the Kondo resonance. ε_0 can be positive or negative depending on whether the position of the extraband is above or below the Fermi level, respectively. Consequently, the overall Seebeck coefficient ($S_{total} = S_N + S_\tau + S_{ph}$) can be estimated. Fig. 5*B* shows that the measured Seebeck coefficient as a function of temperature of MoS_2/*h*-BN device for $n = 2 \times 10^{12}$ cm^{-2} is well captured by this scattering model (more details in *SI Appendix*, Fig. S18). At higher gate voltages, the Fermi level of the MoS_2/*h*-BN sample is raised toward the conduction band, causing resonant scattering to be present only at lower temperatures (Fig. 4*B*). Due to the strong interaction of electrons with the hybridized band through such resonant scattering, the larger S values in the on state of MoS_2 lead to an unusually strong enhancement in the thermoelectric PF ($S^2\sigma$, where σ is calculated from the four-probe sheet conductivity σ_s by considering the thickness of MoS_2) at an equivalent high bulk carrier concentration of $\sim 4.7 \times 10^{18}$ cm^{-3}. This is distinct from the S enhanced only due to the phonon drag effect, which occurs at a much lower doping concentration ($\sim 10^{15}$ cm^{-3}) without a sign change (59), thereby translating to a much lower PF. Fig. 5*C* shows the PF comparison between MoS_2/*h*-BN and MoS_2/SiO_2 samples as a function of temperature. When $T > 120$ K, the PF of the MoS_2/*h*-BN sample is comparable with that of the MoS_2/SiO_2 sample. However, with decreasing temperature, the PF of the MoS_2/*h*-BN sample drops significantly due to the positive S_τ contribution which cancels the contribution from traditional negative S_N. When temperature further decreases, Kondo scattering starts to dominate the thermoelectric transport. A large enhancement in PF up to two orders of magnitude is observed. Such a high PF value of 50 mW m^{-1} K^{-2} (T = 30 to 50 K), originating from band hybridization-enhanced S, is two to four orders of magnitude larger than the PF of other 2D materials (36, 37, 50, 51, 60–62) in the same temperature regime and exhibits the highest PF in 2D materials at all reported temperatures (Fig. 5*D*).

Conclusion

In summary, we discover that band hybridization due to sulfur vacancies exerts a strong influence on the thermoelectric properties of few-layer MoS_2 supported on *h*-BN substrate, whereas these effects are suppressed on SiO_2 substrate. The electric and thermoelectric transport in few-layer MoS_2 on *h*-BN match well with a strongly correlated Kondo-like behavior, leading to a large anomalous positive Seebeck coefficient of 2 mV/K in *n*-type MoS_2 in the on state. Importantly, our work demonstrates that such an effect can be electrostatically tuned to manipulate the Seebeck coefficient, leading to two orders of magnitude enhancement in thermoelectric PF. The ability to exhibit both negative Seebeck (diffusive) and positive Seebeck (band hybridized) coefficients in *n*-type MoS_2 suggests that a singly doped material could be used to fabricate thermoelectric devices, thus bypassing the need for multiple materials in thermoelectric devices. This work also points to the possibility of dopant engineering to make Kondo lattices (63) for nanothermoelectric devices.

Methods

MoS_2 and *h*-BN flakes were separately mechanically exfoliated onto SiO_2/Si substrates. The flakes are then examined by observing the contrast an optical microscope (in both bright-field and dark-field mode) and atomic force microscopy (AFM) to ensure that the surface, geometry, and thickness are suitable for subsequent measurements. MoS_2 flake was transferred onto *h*-BN flakes using standard wet transfer techniques by poly(methyl methacrylate) (PMMA). After that, electrodes were defined by standard electron beam lithography (EBL), followed by deposition of titanium/gold (Ti/Au) with thickness of 3 nm for Ti and 70 nm for Au. Ti was chosen owing to its low work function, comparable to the electron affinity of MoS_2 to form ohmic contacts. The STM measurements were performed using Omicron ultrahigh-vacuum LT-STM (<10^{-10} torr). Before the measurement, the tungsten tip was calibrated by Au (111) crystal. During STM measurements, the sample is grounded through the deposited Ti/Au electrode on top of the MoS_2 flake. The gate electrode is lead out by an aluminum wire. After wire bonding, the MoS_2/*h*-BN sample was annealed at 220 °C in the preparation chamber (<10^{-10} torr) to remove absorbents and form a better contact. STM and STS data were collected at liquid helium temperatures. Constant-current mode was employed to capture STM images, and external lock-in technique was employed to record STS data. Four-probe measurements were employed to eliminate contact resistance and extract a precise electrical conductivity of MoS_2 flakes for different gate voltages. The temperature-dependent mobility is extracted from transfer characteristics, via $\mu_{FE} = \frac{1}{C_{ox}} \frac{d\sigma}{dV_g}$, where $C_{ox} = 12 \times 10^{-9}$ F/cm^2 is the capacitance for 285-nm-thick SiO_2. The sheet conductivity $\left(\sigma_s = \frac{L}{W} G\right)$ is converted from G by considering the length (L) and width (W) of the MoS_2 flake, and electrical conductivity is calculated from $\sigma = \frac{\sigma_s}{d}$ by considering its thickness (d). To measure the Seebeck coefficient $S = V_{TEP}/\Delta T$, a temperature gradient is realized by applying a DC current bias (I) through a metal heater using a source meter (Keithley 6221); therefore, Joule heat and a temperature gradient along the sample are generated. The temperature gradient generates the thermoelectric voltage V_{TEP}, which is measured by a voltmeter (Keithley 6430). As a series of DC current bias with increasing values are applied to the heater, the corresponding V_{TEP} were recorded. The temperature gradient is measured through the four-probe resistance of thermometers.

Data and Materials Availability. All data supporting the findings of this study are available within the article or *SI Appendix*.

ACKNOWLEDGMENTS. This research was supported by Agency for Science, Technology and Research (A*STAR) Pharos Funding from the Science and Engineering Research Council (SERC) (Grant 152 70 00015). K.P.L. acknowledges Ministry of Education (MOE) Tier 3 Grant "Two-dimensional crystal quantum exciton photonic," Project MOE2018-T3-1-005. C.-W.Q. acknowledges the A*STAR SERC Pharos Grant 152 70 00014 with Project R-263-000-B91-305. A.H.C.N. acknowledges the National Research Foundation (NRF) Competitive Research Programme Award R-144-000-295-281. We also thank Professor Zheng Yi for the helpful discussion and comments.

1. G. J. Snyder, E. S. Toberer, Complex thermoelectric materials. *Nat. Mater.* **7**, 105–114 (2008).
2. J. Wu, Y. Chen, J. Wu, K. Hippalgaonkar, Perspectives on thermoelectricity in layered and 2D materials. *Adv. Electron. Mater.* **14**, 1800248 (2018).
3. C. Chang *et al*., 3D charge and 2D phonon transports leading to high out-of-plane ZT in n-type SnSe crystals. *Science* **360**, 778–783 (2018).
4. L. D. Zhao *et al*., Ultralow thermal conductivity and high thermoelectric figure of merit in SnSe crystals. *Nature* **508**, 373–377 (2014).
5. F. Ghahari *et al*., Enhanced thermoelectric power in graphene: Violation of the Mott relation by inelastic scattering. *Phys. Rev. Lett.* **116**, 136802 (2016).
6. J. H. Chen, L. Li, W. G. Cullen, E. D. Williams, M. S. Fuhrer, Tunable Kondo effect in graphene with defects. *Nat. Phys.* **7**, 535–538 (2011).
7. A. Demion, A. D. Verga, Nonlinear electric transport in graphene with magnetic disorder. *Phys. Rev. B Condens. Matter Mater. Phys.* **90**, 1–9 (2014).
8. D. Xiao, G. Bin Liu, W. Feng, X. Xu, W. Yao, Coupled spin and valley physics in monolayers of MoS 2 and other group-VI dichalcogenides. *Phys. Rev. Lett.* **108**, 1–5 (2012).
9. Q. H. Wang, K. Kalantar-Zadeh, A. Kis, J. N. Coleman, M. S. Strano, Electronics and optoelectronics of two-dimensional transition metal dichalcogenides. *Nat. Nanotechnol.* **7**, 699–712 (2012).
10. Z. Y. Zhu, Y. C. Cheng, U. Schwingenschlögl, Giant spin-orbit-induced spin splitting in two-dimensional transition-metal dichalcogenide semiconductors. *Phys. Rev. B Condens. Matter Mater. Phys.* **84**, 1–5 (2011).
11. K. Komider, J. W. González, J. Fernández-Rossier, Large spin splitting in the conduction band of transition metal dichalcogenide monolayers. *Phys. Rev. B Condens. Matter Mater. Phys.* **88**, 1–7 (2013).
12. L. Cai *et al*., Vacancy-induced ferromagnetism of MoS2 nanosheets. *J. Am. Chem. Soc.* **137**, 2622–2627 (2015).
13. A. S. Rodin, A. H. C. Neto, Localized magnetic states in two-dimensional semiconductors. *Phys. Rev. B* **97**, 235428 (2018).
14. J. Zhang *et al*., Magnetic molybdenum disulfide nanosheet films. *Nano Lett.* **7**, 2370–2376 (2007).
15. H. Pan, Y. W. Zhang, Tuning the electronic and magnetic properties of MoS 2 nanoribbons by strain engineering. *J. Phys. Chem. C* **116**, 11752–11757 (2012).
16. S. W. Han *et al*., Electron beam-formed ferromagnetic defects on MoS_2 surface along 1 T phase transition. *Sci. Rep.* **6**, 38730 (2016).
17. K. F. Mak, K. He, J. Shan, T. F. Heinz, Control of valley polarization in monolayer MoS2 by optical helicity. *Nat. Nanotechnol.* **7**, 494–498 (2012).

APPLIED PHYSICAL SCIENCES

Downloaded at Ukraine: PNAS Sponsored on June 13, 2020

18. J. Pető *et al*., Spontaneous doping of the basal plane of MoS_2 single layers through oxygen substitution under ambient conditions. *Nat. Chem.* **10**, 1246–1251 (2018).
19. Y. L. Huang *et al*., Bandgap tunability at single-layer molybdenum disulphide grain boundaries. *Nat. Commun.* **6**, 6298 (2015).
20. J. Hong *et al*., Exploring atomic defects in molybdenum disulphide monolayers. *Nat. Commun.* **6**, 6293 (2015).
21. M. Neupane *et al*., Surface electronic structure of the topological Kondo-insulator candidate correlated electron system SmB_6. *Nat. Commun.* **4**, 2991 (2013).
22. Y. Cai, H. Zhou, G. Zhang, Y. Zhang, Modulating carrier density and transport properties of MoS2 by organic molecular doping and defect engineering. *Chem. Mater.* **28**, 8611–8621 (2016).
23. R. R. Nair *et al*., Spin-half paramagnetism in graphene induced by point defects. *Nat. Phys.* **8**, 199–202 (2012).
24. B. W. H. Baugher, H. O. H. Churchill, Y. Yang, P. Jarillo-Herrero, Intrinsic electronic transport properties of high-quality monolayer and bilayer MoS2. *Nano Lett.* **13**, 4212–4216 (2013).
25. B. Radisavljevic, A. Kis, Mobility engineering and a metal-insulator transition in monolayer MoS_2. *Nat. Mater.* **12**, 815–820 (2013).
26. H. Schmidt *et al*., Transport properties of monolayer MoS2 grown by chemical vapor deposition. *Nano Lett.* **14**, 1909–1913 (2014).
27. X. Cui *et al*., Multi-terminal transport measurements of MoS2 using a van der Waals heterostructure device platform. *Nat. Nanotechnol.* **10**, 534–540 (2015).
28. B. Peng *et al*., Thermal conductivity of monolayer MoS2, MoSe2, and WS2: Interplay of mass effect, interatomic bonding and anharmonicity. *RSC Advances* **6**, 5767–5773 (2016).
29. D. K. Efetov, P. Kim, Controlling electron-phonon interactions in graphene at ultrahigh carrier densities. *Phys. Rev. Lett.* **105**, 256805 (2010).
30. L. Kouwenhoven, L. Glazman, Revival of the Kondo effect. *Phys. World* **14**, 33–38 (2001).
31. N. Grewe, F. Steglich, “Heavy fermions” in *Handbook on the Physics and Chemistry of Rare Earths*, K. A. Gschneidner Jr., L. Eyring, Eds. (Elsevier Science Publishers, Amsterdam, 1991), pp. 343–474.
32. P. Phillips, *Advanced solid State Physics* (Westview Press, 2003).
33. R. Gumeniuk, W. Schnelle, K. O. Kvashnina, A. Leithe-Jasper, Kondo effect and thermoelectric transport in CePd3Be x. *J. Phys. Condens. Matter* **28**, 165603 (2016).
34. D. Goldhaber-Gordon *et al*., From the Kondo regime to the mixed-valence regime in a single-electron transistor. *Phys. Rev. Lett.* **81**, 5225–5228 (1998).
35. T. A. Costi, A. C. Hewson, V. Zlatic, Transport coefficients of the Anderson model via the numerical renormalization group. *J. Phys. Condens. Matter* **6**, 2519 (1994).
36. K. Hippalgaonkar *et al*., High thermoelectric power factor in two-dimensional crystals of MoS2. *Phys. Rev. B* **95**, 115407 (2017).
37. M. Kayyalha, J. Maassen, M. Lundstrom, L. Shi, Y. P. Chen, Gate-tunable and thickness-dependent electronic and thermoelectric transport in few-layer MoS2. *J. Appl. Phys.* **120**, 134305 (2016).
38. M. Yarali *et al*., Effects of defects on the temperature-dependent thermal conductivity of suspended monolayer molybdenum disulfide grown by chemical vapor deposition. *Adv. Funct. Mater.* **27**, 1704357 (2017).
39. A. Aiyiti *et al*., Thermal conductivity of suspended few-layer MoS_2. *Nanoscale* **10**, 2727–2734 (2018).
40. H. Takahashi *et al*., Colossal Seebeck effect enhanced by quasi-ballistic phonons dragging massive electrons in FeSb2. *Nat. Commun.* **7**, 12732 (2016).
41. T. Cheiwchanchamnangij, W. R. L. Lambrecht, Quasiparticle band structure calculation of monolayer, bilayer, and bulk MoS2. *Phys. Rev. B Condens. Matter Mater. Phys.* **85**, 205302 (2012).
42. M. Cutler, N. F. Mott, Observation of Anderson localization in an electron gas. *Phys. Rev.* **181**, 1336–1340 (1969).
43. M. Lundstrom, *Fundamentals of Carrier Transport* (Cambridge University Press, ed. 2, 2000).
44. H. K. Ng, D. Chi, K. Hippalgaonkar, Effect of dimensionality on thermoelectric powerfactor of molybdenum disulfide. *J. Appl. Phys.* **121**, 204303 (2017).
45. G. Wang, L. Endicott, H. Chi, P. Lošt’ák, C. Uher, Tuning the temperature domain of phonon drag in thin films by the choice of substrate. *Phys. Rev. Lett.* **111**, 046803 (2013).
46. H. Takahashi, R. Okazaki, Y. Yasui, I. Terasaki, Low-temperature magnetotransport of the narrow-gap semiconductor FeSb2. *Phys. Rev. B Condens. Matter Mater. Phys.* **84**, 205215 (2011).
47. B. C. Sales *et al*., Transport, thermal, and magnetic properties of the narrow-gap semiconductor CrSb2. *Phys. Rev. B Condens. Matter Mater. Phys.* **86**, 235136 (2012).
48. C. Herring, Theory of the thermoelectric power of semiconductors. *Phys. Rev.* **96**, 1163–1187 (1954).
49. Y. Cai, J. Lan, G. Zhang, Y. Zhang, Lattice vibrational modes and phonon thermal conductivity of monolayer MoS2. *Phys. Rev. B Condens. Matter Mater. Phys.* **89**, 035438 (2014).
50. J. Duan *et al*., High thermoelectricpower factor in graphene/hBN devices. *Proc. Natl. Acad. Sci. U.S.A.* **113**, 14272–14276 (2016).
51. Y. Saito *et al*., Gate-tuned thermoelectric power in black phosphorus. *Nano Lett.* **16**, 4819–4824 (2016).
52. L. Yang *et al*., Distinct signatures of electron-phonon coupling observed in the lattice thermal conductivity of $NbSe_3$ nanowires. *Nano Lett.* **19**, 415–421 (2019).
53. D. Dominko, Optical phonon drag and variable range hopping mechanisms of thermoelectric power generation in charge density wave system o-TaS 3. arXiv:1408.6190 (26 August 2014).
54. A. K. Mitchell, L. Fritz, Kondo effect with diverging hybridization: Possible realization in graphene with vacancies. *Phys. Rev. B Condens. Matter Mater. Phys.* **88**, 075104 (2013).
55. Y. Jiang *et al*., Inducing Kondo screening of vacancy magnetic moments in graphene with gating and local curvature. *Nat. Commun.* **9**, 2349 (2018).
56. P. Sun, F. Steglich, Nernst effect: Evidence of local Kondo scattering in heavy fermions. *Phys. Rev. Lett.* **110**, 216408 (2013).
57. P. Sun *et al*., Large Seebeck effect by charge-mobility engineering. *Nat. Commun.* **6**, 7475 (2015).
58. L. L. Hirst, Electronic properties of 4f substances at configuration crossover. *Phys. Rev. B* **15**, 1–9 (1977).
59. J. Zhou *et al*., Ab initio optimization of phonon drag effect for lower-temperature thermoelectric energy conversion. *Proc. Natl. Acad. Sci. U.S.A.* **112**, 14777–14782 (2015).
60. M. Yoshida *et al*., Gate-optimized thermoelectric power factor in ultrathin WSe2 single crystals. *Nano Lett.* **16**, 2061–2065 (2016).
61. C. Wan *et al*., Flexible n-type thermoelectric materials by organic intercalation of layered transition metal dichalcogenide TiS2. *Nat. Mater.* **14**, 622–627 (2015).
62. C. Wan *et al*., Flexible thermoelectric foil for wearable energy harvesting. *Nano Energy* **30**, 840–845 (2016).
63. Y. Jiang, Y. N. Zhang, J. X. Cao, R. Q. Wu, W. Ho, Real-space imaging of Kondo screening in a two-dimensional O2 lattice. *Science* **333**, 324–328 (2011).
64. P. Gegenwart, Q. Si, F. Steglich, Quantum criticality in heavy-fermion metals. *Nat. Phys.* **4**, 186–197 (2008).

Downloaded at Ukraine: PNAS Sponsored on June 13, 2020